



# Multiwavelength Observations of a New Redback Millisecond Pulsar Candidate: 3FGL J0954.8–3948

Kwan-Lok Li<sup>1</sup> , Xian Hou<sup>2,3</sup> , Jay Strader<sup>1</sup> , Jumpei Takata<sup>4</sup> , Albert K. H. Kong<sup>5</sup> , Laura Chomiuk<sup>1</sup> , Samuel J. Swihart<sup>1</sup> , Chung Yue Hui<sup>6</sup>, and K. S. Cheng<sup>7</sup>

<sup>1</sup> Department of Physics and Astronomy, Michigan State University, East Lansing, MI 48824, USA; [liliray@msu.edu](mailto:liliray@msu.edu)

<sup>2</sup> Yunnan Observatories, Chinese Academy of Sciences, Kunming, 650216, People's Republic of China

<sup>3</sup> Key Laboratory for the Structure and Evolution of Celestial Objects, Chinese Academy of Sciences, Kunming, 650216, People's Republic of China

<sup>4</sup> School of Physics, Huazhong University of Science and Technology, Wuhan 430074, People's Republic of China

<sup>5</sup> Institute of Astronomy, National Tsing Hua University, Hsinchu 30013, Taiwan

<sup>6</sup> Department of Astronomy and Space Science, Chungnam National University, Daejeon 34134, Republic of Korea

<sup>7</sup> Department of Physics, The University of Hong Kong, Pokfulam Road, Hong Kong

Received 2018 June 5; revised 2018 June 23; accepted 2018 July 5; published 2018 August 23

## Abstract

We present a multiwavelength study of the unassociated *Fermi* Large Area Telescope (LAT) source, 3FGL J0954.8–3948, which is likely the  $\gamma$ -ray counterpart of a 9.3 hr binary in the field. With more than 9 years of Pass 8 LAT data, we updated the  $\gamma$ -ray spectral properties and the LAT localization of the  $\gamma$ -ray source. While the binary lies outside the cataloged 95% error ellipse, the optimized LAT ellipse is  $0^\circ.1$  closer and encloses the binary. The system is likely spectrally hard in X-rays (photon index  $\Gamma_X = 1.4^{+1.2}_{-1.0}$ ) with orbital modulations detected in optical, ultraviolet, and possibly X-rays. A steep spectrum radio counterpart (spectral index  $\alpha \approx -1.6$ ) is also found in the TIFR GMRT Sky Survey, implying that it is a pulsar system. We obtained a series of SOAR and Gemini spectroscopic observations in 2017/2018, which show a low-mass secondary orbiting in a close circular orbit with  $K_2 = 272 \pm 4 \text{ km s}^{-1}$  under strong irradiation by the primary compact object. All the observations as well as the modeling of the X/ $\gamma$ -ray high-energy emission suggest that 3FGL J0954.8–3948 is a redback millisecond pulsar in a rotation-powered state.

**Key words:** binaries: close – gamma rays: stars – pulsars: general – X-rays: binaries

## 1. Introduction

Redback and black widow millisecond pulsars (MSPs) are unique subclasses of pulsar binaries which have compact orbits (periods of  $\lesssim 1$  days) and very-low-mass companions ( $M_2 = 0.1\text{--}0.4 M_\odot$  for redback and  $< 0.1 M_\odot$  for black widow; Chen et al. 2013; Roberts 2013). With separations of just a few  $R_\odot$  or less, the primary pulsars heavily ablate the secondary stars with high-power radiation and pulsar winds, potentially explaining how isolated MSPs are formed (van den Heuvel & van Paradijs 1988). They became even more interesting recently as three redback MSPs (also known as transitional MSPs), M281 (Papitto et al. 2013), PSR J1023+0038 (Archibald et al. 2009; Patruno et al. 2014; Stappers et al. 2014), and PSR J1227–4853 (Roy et al. 2015), have shown remarkable transitions between the low-mass X-ray binary (LMXB) state and the radio pulsar state, which could be an important piece of evidence for the recycling explanation for MSP formation (Alpar et al. 1982).

In the *Fermi* Large Area Telescope (LAT) third source catalog (3FGL; Acero et al. 2015), over 1000  $\gamma$ -ray sources are without definitive associations at other wavelengths. On the basis of previous work (e.g., Abdo et al. 2013), some of these unassociated *Fermi*-LAT sources are likely to be redback and black widow MSPs. In fact, recent coordinated multiwavelength searches have identified at least nine unassociated *Fermi*-LAT sources as promising redback/black widow candidates, including<sup>8</sup>: 3FGL J0838.8–2829 (Halpern et al. 2017), 3FGL J0212.1+5320

(Li et al. 2016; Linares et al. 2017), 3FGL J0427.9–6704 (Strader et al. 2016), 3FGL J2039.6–5618 (Romani 2015; Salvetti et al. 2015), 3FGL J1544.6–1125 (Bogdanov & Halpern 2015), 2FGL J1653.6–0159 (Kong et al. 2014; Romani et al. 2014), 1FGL J0523.5–2529 (Strader et al. 2014), 2FGL J1311.7–3429 (Kataoka et al. 2012; Romani 2012), and 1FGL J2339.7–0531 (Romani & Shaw 2011; Kong et al. 2012), at least two of which, PSR J1311-3430 (Pletsch et al. 2012) and PSR J2339-0533 (Pletsch & Clark 2015), have been confirmed as MSPs. It is also worth mentioning that 3FGL J0427.9–6704 and 3FGL J1544.6–1125 are  $\gamma$ -ray-emitting LMXBs that are good candidates for transitional MSPs.

3FGL J0954.8–3948 is a bright unassociated *Fermi*-LAT source in 3FGL, detected in 0.1–100 GeV with a detection significance of  $19\sigma$  (Acero et al. 2015). It first appeared in the *Fermi*-LAT first source catalog (1FGL; Abdo et al. 2010), and subsequently in the *Fermi*-LAT second source catalog (2FGL; Nolan et al. 2012). The  $\gamma$ -ray source resembles other  $\gamma$ -ray pulsars with low source variability (its chi-squared variability index of 51 with 47 degrees of freedom is consistent with a steady source) and a significantly curved  $\gamma$ -ray spectrum (Abdo et al. 2013). Both features suggest that 3FGL J0954.8–3948 could be a  $\gamma$ -ray pulsar. Indeed, Saz Parkinson et al. (2016) found that 3FGL J0954.8–3948 is a strong MSP candidate using statistical and machine learning techniques. Drake et al. (2017) suggested a binary with an orbital period of 9.3 hr, named SSS J095527.8–394752, to be a promising counterpart to 1FGL J0955.2–3949. In addition, a bright radio counterpart possibly associated with the binary was independently discovered by Frail et al. (2016). However, these counterparts were later

<sup>8</sup> The list does not include 2FGL J0846.0+2820 (Swihart et al. 2017) and 1FGL J1417.7–4407 (Strader et al. 2015), which have giant secondaries with orbital periods of 8.1 days and 5.4 days, respectively. The latter was confirmed as an MSP (PSR J1417–4402; Camilo et al. 2016)

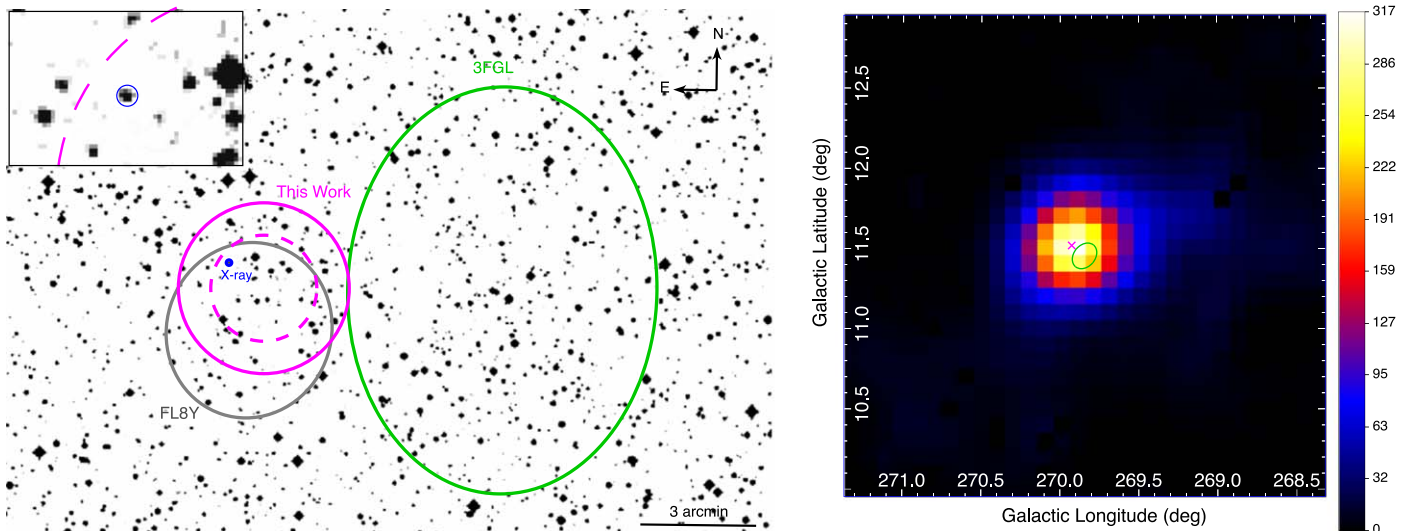


**Figure 1.** Left: DSS-1 image of the field of 3FGL J0954.8–3948 overlapped with green and gray ellipses as the 95% error regions of 3FGL J0954.8–3948 in 3FGL and FL8Y, respectively; magenta concentric circles as the new LAT error circles in 68% (dashed) and 95% (solid) confidence levels (PLEpCutoff spectral model assumed); and a small blue circle as the 90% error circle of 1SXPS J095527.8–394750. The upper left inset box is the zoomed-in view of the optical counterpart, SSS J095527.8–394752. Right: TS map of 3FGL J0954.8–3948 (in Galactic coordinates) with the 3FGL 95% error ellipse (green) and the new LAT best-fit position (magenta cross). The new position is consistent with the brightest central pixel, which signifies the highest source detection significance.

**Table 1**  
Fermi-LAT Properties of 3FGL J0954.8–3948

Model	3FGL Position		Relocalization (1–100 GeV)				Best-fit Parameters (0.1–100 GeV)				
	$-\log \mathcal{L}$	TS	R.A. <sup>a</sup> (degree)	Decl. <sup>a</sup> (degree)	95% Radius (degree)	$-\log \mathcal{L}$	TS	$\Gamma_g$	$E_c$ (GeV)	$\beta$	$F_{\text{ph}}$ ( $10^{-8} \text{ cm}^{-2} \text{ s}^{-1}$ )
PLEpCutoff	125311.76	309	148.8462	−39.8089	0.0369	125289.08	355	$2.2 \pm 0.1$	$4.5 \pm 1.2$	...	$3.1 \pm 0.2$
LogParabola	125312.25	309	148.8459	−39.8087	0.0368	125289.84	353	$2.2 \pm 0.1$	...	$0.13 \pm 0.04$	$2.9 \pm 0.2$

**Note.**

<sup>a</sup> The coordinates are in the J2000 frame.

found to be outside the 3FGL error ellipse, and the association therefore remains questionable until now.

In this paper, we present multiwavelength observations of 3FGL J0954.8–3948, with which we show that SSS J095527.8–394752 is still likely to be the counterpart of the  $\gamma$ -ray source. Furthermore, the observed timing and spectral properties are in agreement with the suggestion of Drake et al. (2017) that 3FGL J0954.8–3948 is a new member of the group of reback MSPs.

## 2. Fermi-LAT Gamma-Ray Analysis

Before searching for the X-ray/optical counterparts, we first relocalized 3FGL J0954.8–3948 in  $\gamma$ -rays taking advantage of the Pass 8 LAT data (Atwood et al. 2013) with a timespan of more than 9 years, whose performance has been much improved over the 4 years of Pass 7 data used in 3FGL. This would in principle yield a more precise  $\gamma$ -ray position with a more restricted error circle.

The LAT events and the spacecraft data were downloaded from the Fermi Science Support Center (FSSC).<sup>9</sup> The data set covers the time range of 2008 August 4–2017 December 16 with reconstructed energy in 0.1–100 GeV. We selected SOURCE

class events (Front and Back) but excluded those with a zenith angle larger than  $90^\circ$  or a rocking angle larger than  $52^\circ$  to avoid Earth limb contamination. The region of interest (ROI) was centered at  $(\alpha, \delta) = (148^\circ 712, -39^\circ 809)$ , which is the 3FGL position of 3FGL J0954.8–3948. All the 3FGL sources located within a  $20^\circ$  radius circle at the center were included to build a spatial and spectral model for the  $\gamma$ -ray emission in the field. The model also includes the latest Galactic interstellar emission model (gll\_iem\_v06.fits) and the isotropic emission spectrum (iso\_P8R2\_SOURCE\_V6\_v06.txt), of which the latter takes the extragalactic emission and the residual instrumental background into account (Acero et al. 2016).

With the latest instrument response function P8R2\_SOURCE\_V6, model fitting was performed by the maximum likelihood method (Mattox et al. 1996), which is integrated into the Fermi Science Tools available at FSSC. In addition, the fermipy package<sup>10</sup> developed within the LAT collaboration was used to facilitate the analysis (Wood et al. 2017). Under the framework, the significance of a certain source is characterized by Test Statistic (TS),

$$\text{TS} = 2(\log \mathcal{L} - \log \mathcal{L}_0),$$

<sup>9</sup> <http://fermi.gsfc.nasa.gov/ssc/>

<sup>10</sup> <http://fermipy.readthedocs.io/en/latest/index.html>

where  $\log \mathcal{L}$  and  $\log \mathcal{L}_0$  are the logarithms of the maximum likelihood of the complete source model and of the null hypothesis model (i.e., the source model without the certain source), respectively.

The localization fit was performed at  $>1$  GeV to benefit from the improved angular resolution and the reduced background contamination. We first performed an initial fit with a  $14^\circ \times 14^\circ$  ROI, by allowing the background diffuse components as well as all the sources located  $<5^\circ$  from 3FGL J0954.8–3948 to vary. Given the  $\sim 4\sigma$  evidence for spectral curvature of 3FGL J0954.8–3948 in 3FGL, we employed two curved spectral models for it,

$$\text{PLExpCutoff: } \frac{dN}{dE} \propto E^{-\Gamma_g} \exp\left(-\frac{E}{E_c}\right)$$

and

$$\text{LogParabola: } \frac{dN}{dE} \propto \left(\frac{E}{E_b}\right)^{-(\Gamma_g + \beta \log(E/E_b))}$$

where  $\Gamma_g$  serves as the photon index for both models,  $E_c$  characterizes the cutoff energy for PLEXPcutoff,  $\beta$  defines the degree of curvature for LogParabola, and  $E_b$  is a fixed scale parameter. Both models give good fits to the data, and PLEXPcutoff is slightly preferred over LogParabola by  $1\sigma$ . Three parameter-fixed  $\gamma$ -ray sources located outside the  $5^\circ$  region, 3FGL J0928.9–3530, 3FGL J0937.1–4544c, and 3FGL J1007.4–3334, were not well modeled in the first round and a second iteration was done with their normalization parameters freed.

Taking the best-fit source model from the aforementioned processes as the input, we relocalized 3FGL J0954.8–3948 using the ‘‘Source localization’’ function in `fermipy` for both LogParabola and PLEXPcutoff models. The spectral parameters of all the sources, except the Galactic/Isotropic diffuse components and 3FGL J0954.8–3948, were fixed during the localization, although we found that freeing the normalizations of the background diffuse components had no significant effect on the localization result. Table 1 summarizes the best localization parameters of 3FGL J0954.8–3948 for PLEXPcutoff and LogParabola. There is no obvious difference between the localizations from LogParabola and PLEXPcutoff, but the PLEXPcutoff version is slightly favored given the smaller  $-\log \mathcal{L}$  of the best fit. Figure 1 shows the new  $\gamma$ -ray localization of 3FGL J0954.8–3948 (PLEXPcutoff) on the DSS-1 image and the TS map of the field. Compared with the 95% error ellipse of 3FGL J0954.8–3948 presented in 3FGL (i.e.,  $5'.3$  and  $4'.0$  for the semimajor and semiminor axes, respectively), the updated LAT position is shifted by  $6'.2$  to  $(\alpha, \delta) = (148^\circ 8462, -39^\circ 8089)$  with a much improved 95% error radius of  $2'.2$  (Figure 1). Using this best-fit position, broadband spectral fitting in the energy range of 0.1–100 GeV was also performed for both PLEXPcutoff and LogParabola, and the best-fit parameters are listed in Table 1.

High long-term  $\gamma$ -ray flux variability is a common feature of transitional MSPs. To examine this possibility for 3FGL J0954.8–3948, we computed a long-term light curve with 90 day binning in the energy range of 0.1–100 GeV (Figure 2). For each time bin, the flux was calculated independently using the likelihood analysis. In the source model used, the spectral shapes of all sources (including 3FGL J0954.8–3948) located within  $5^\circ$  from 3FGL J0954.8–3948 were fixed according to their best-fit models determined

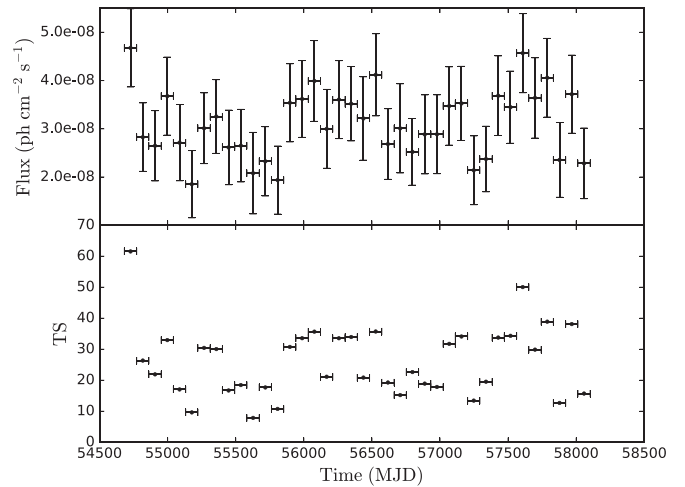


**Figure 2.** Light curve and TS evolution for 3FGL J0954.8–3948 in the energy range of 0.1–100 GeV with 90 day binning.

previously (i.e., only normalizations were allowed to vary). Upper limits at 95% confidence level were calculated when 3FGL J0954.8–3948 had  $\text{TS} < 4$ . In addition, we followed the method presented in Acero et al. (2015) to obtain the variability significance of 3FGL J0954.8–3948, which is just  $0.4\sigma$  (for 37 degrees of freedom). The  $\gamma$ -ray emission is thus considered to be stable on a timescale of a few months, ruling out the possibility of 3FGL J0954.8–3948 being a transitional MSP within the LAT mission.

### 3. Neil Gehrels Swift Observations

*Swift* has observed the field of 3FGL J0954.8–3948 10 times between 2010 March and 2017 March. Five of the observations taken in 2015 are with short exposure times less than 400 s, while the other five have relatively long exposures (Table 2). In the stacked X-ray Telescope (XRT) image, only one X-ray source at  $\alpha(\text{J2000}) = 09^{\text{h}}55^{\text{m}}28^{\text{s}}.40$ ,  $\delta(\text{J2000}) = -39^\circ 48' 02''.1$  (90% positional uncertainty:  $3''.5$ ) is detected within the new 95% LAT error circle (Figure 1). The X-ray source is listed as 1SXPS J095527.8–394750 in the *Swift*-XRT point source catalog (1SXPS; Evans et al. 2014), in which only part of the observation was analyzed. We therefore reanalyzed the source with all 10 observations to improve the spectral fitting as well as the long-term X-ray light curve of the source. As the field is not crowded and no other bright X-ray source is found around the target, we simply used the *Swift*-XRT online tools<sup>11</sup> provided by the *Swift* team (Evans et al. 2007, 2009) to perform the following XRT analyses.

While 1SXPS J095527.8–394750 is significantly detected, the low photon statistics only allow a basic spectral analysis (i.e., only 32 photons collected within a  $20''$  radius circular region). To deal with the low-count spectrum, we used XSPEC (version 12.9.1m) with *W-statistic* (a modified version of *C-statistic*; Cash 1979) in the fitting process. In addition, we binned the spectrum accordingly so that every bin contains at least one source count as the development team suggested. A simple absorbed power law is assumed and the best-fit parameters are  $N_{\text{H}} = 5.2_{-5.0}^{+8.9} \times 10^{21} \text{ cm}^{-2}$ ,  $\Gamma_{\text{X}} = 1.4_{-1.0}^{+1.2}$ , and  $F_{0.3-10 \text{ keV}} = 3.0_{-1.0}^{+3.6} \times 10^{-13} \text{ erg cm}^{-2} \text{ s}^{-1}$

<sup>11</sup> [http://www.swift.ac.uk/user\\_objects/](http://www.swift.ac.uk/user_objects/)

**Table 2**  
Swift Observations of 3FGL J0954.8–3948

Swift ObsID	Date	BJD (start time)	XRT Exposure (s)	XRT Count Rate <sup>a</sup> ( $10^{-3}$ cts $s^{-1}$ )	UVOT Filter	Magnitude <sup>a</sup> (Vega)
00031664001	2010 Mar 24	2455279.5230275	3557	$5.0 \pm 1.4$	UVW1	$20.24 \pm 0.13$
00084699001	2015 Feb 04	2457057.7715524	238	$<27.0^b$	UVW2	$>20.40$
00084699002	2015 Feb 16	2457070.4008172	145	$<37.0^b$	UVW2	$>20.33$
00084699003	2015 Jun 21	2457195.0878701	186	$<24.7^b$	UVM2	$>20.78$
00084699004	2015 Aug 07	2457242.3099548	278	$<22.5^b$	UVW2	$>20.47$
00084699005	2015 Aug 12	2457247.3567788	356	$<36.1^b$	UVM2	$>20.36$
00084699006	2015 Aug 19	2457254.1462335	1578	$<8.7^b$	UVW2	$20.07 \pm 0.19$
00084699007	2015 Aug 24	2457258.9278091	1091	$4.4^{+2.8}_{-2.0}$	UVM2	$20.01 \pm 0.24$
00034854001	2016 Dec 22	2457744.5423559	1785	$3.4^{+2.0}_{-1.3}$	U	$18.97 \pm 0.07$
00034854002	2017 Mar 09	2457821.8875329	2008	$3.9^{+2.1}_{-1.6}$	UVW2	$>21.74$

**Notes.**

<sup>a</sup> The upper limits listed are in 95% confidence level.

<sup>b</sup> The source is detected in the stacked Swift-XRT image with  $2.1^{+1.6}_{-1.2} \times 10^{-3}$  cts  $s^{-1}$ .

(absorption corrected; all the uncertainties listed are in 90% confidence interval). Although it is not significant, the best-fit  $N_H$  is a few times higher than the Galactic value of  $1.34 \times 10^{21}$   $\text{cm}^{-2}$  (Kalberla et al. 2005), which may indicate an intrinsic absorption of the system. If a value closer to the Galactic value is used, e.g.,  $N_H = 10^{21}$   $\text{cm}^{-2}$ , the best-fit parameters change to  $\Gamma_X = 0.8 \pm 0.5$  and  $F_{0.3-10 \text{ keV}} = 3.1^{+1.9}_{-1.2} \times 10^{-13}$   $\text{erg cm}^{-2} \text{ s}^{-1}$ . We also tried the thermal model *mekal*, which requires an unreasonably high temperature of  $kT \approx 30$  keV to describe the spectrum. Given the poor data quality of the spectrum, we did not try any complex models with two or multiple emission components.

Five XRT observations got only low exposure (i.e., much less than 1 ks) and the X-ray source was therefore undetected in these data sets. Surprisingly, we also found that the source was undetected in a “deep” observation taken on 2015 August 19 with an exposure time of about 1.6 ks (Table 2). Within a  $47''$  radius circular region centered at the source position (corresponding to 90% of the encircled energy fraction of XRT at 1.5 keV; Moretti et al. 2005), only one photon (which is located near the edge of the region) was detected in this 1.6 ks observation. Even assuming that only this event is from the source, the inferred count rate is much lower than the measurements in 2010 and 2015–2017; for example, seven source counts would have been detected in a 1.6 ks observation with the count rate of  $4.4 \times 10^{-3}$  cts  $s^{-1}$  measured five days later (Table 2). Using a Bayesian approach (Kraft et al. 1991), we computed 95% upper limits for all the nondetections. As expected, the upper limits for data with  $<1$  ks are not very much constraining (i.e., a few  $\times 10^{-2}$  cts  $s^{-1}$ , while the average count rate of the four individual detections is about  $4 \times 10^{-3}$  cts  $s^{-1}$ ). The upper limit for the 1.6 ks data is deeper (i.e.,  $<8.7 \times 10^{-3}$  cts  $s^{-1}$ ), but still insufficient to clarify whether the low-count-rate measurement is physically or statistically based. For a deeper constraint, we combined all the six XRT observations, and the X-ray source can be marginally detected in the stacked image with  $2.1^{+1.6}_{-1.2} \times 10^{-3}$  cts  $s^{-1}$ . Although this marginal detection shows a  $\sim 50\%$  decrease on flux in the period from 2015 February 04 through August 19, the variability is not statistically significant (i.e., less than  $2\sigma$ ). To check whether this variability was seen at other frequencies, we performed a *Fermi*-LAT analysis with the data collected between 2015 February 04 and August 19,

and the  $\gamma$ -ray flux (100 MeV–100 GeV) did not vary significantly. In UV, there are some Ultraviolet/Optical Telescope (UVOT) images taken simultaneously with the XRT observations. Although the UVOT magnitudes (obtained by aperture photometry using the *uvotsource* task in HEASOFT v6.22) significantly changed over time (Table 2), this was due to the orbital modulation (Figure 3; will be discussed in the coming sections).

#### 4. Catalina Surveys Data

In the CSS Periodic Variable Star Catalog, Drake et al. (2017) identified a  $V_{\text{CSS}} = 18.45$  mag candidate optical counterpart for the X-ray system, SSS J095527.8–394752 (the accurate *Gaia* position in the Data Release 2:  $\alpha(\text{J2000}) = 09^{\text{h}}55^{\text{m}}27^{\text{s}}.8090842 \pm 0.11$  mas,  $\delta(\text{J2000}) = -39^{\circ}47'52''.29613 \pm 0.13$  mas; Gaia Collaboration et al. 2016, 2018), which is the only optical source located within the 90% positional uncertainty of 1SXPS J095527.8–394750. The source was classified as a non-EA (Algol type) eclipsing binary with  $P_{\text{CSS}} = 0.387330$  day (about 9.3 hr). The photometric data (186 individual exposures) obtained from the Catalina Surveys Data Release 2 (Drake et al. 2009)<sup>12</sup> shows a clear sinusoidal-like profile at 9.3 hr (Figure 3; the light curve has been barycentric corrected to the Barycentric Dynamical Time (TDB) system; Eastman et al. 2010). We fit the data with a sinusoidal function and the best-fit mean magnitude is  $V_{\text{CSS}} \approx 18.4$  mag with a peak-to-peak amplitude of  $\Delta V_{\text{CSS}} \approx 1.2$  mag. For the XRT variability discussed in Section 3, no further investigation is allowed on the CSS optical light curve as it does not cover the time of interest.

#### 5. SOAR and Gemini South Spectroscopy

We obtained optical spectroscopy of the source using the Goodman Spectrograph (Clemens et al. 2004) on the SOAR telescope (UT 2017 July 11 to 2018 January 22) and using GMOS-S on the Gemini South telescope (2017 December 8 to 19). The SOAR spectra all used a  $4001 \text{ mm}^{-1}$  grating with a  $0''.95$  slit, giving a FWHM resolution of about  $5.3 \text{ \AA}$ . Most of the SOAR spectra covered a wavelength range of about

<sup>12</sup> All the CSS data were taken unfiltered.

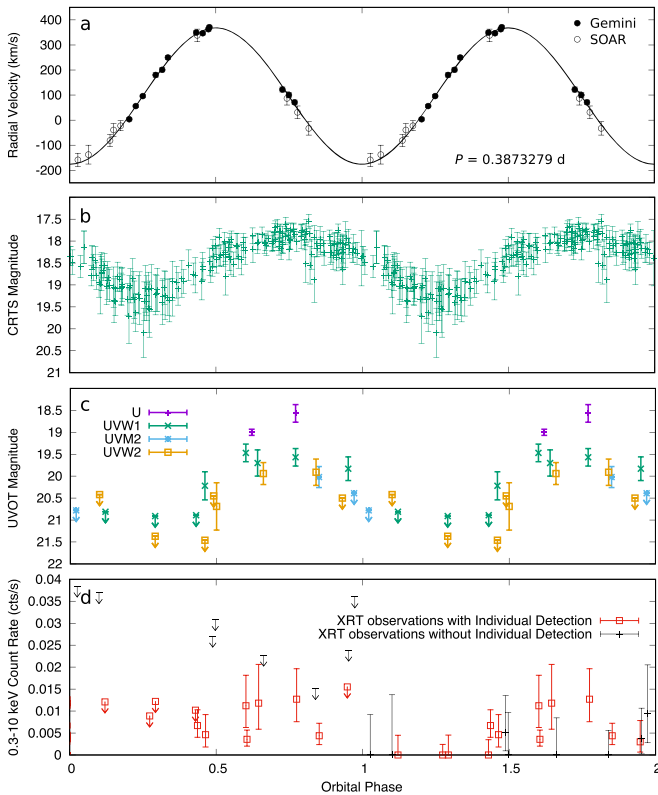


**Figure 3.** The figure shows (a) the radial velocities curve, (b) the CSS light curve, (c) the UVOT light curves, and (d) the *Swift*-XRT (0.3–10 keV) light curve (binned per orbit) of 3FGL J0954.8–3948, which are all folded on the orbital period of  $P_{\text{joint}} = 0.3873279$  days with phase zero at BJD 2458097.94395 (the ascending node). Two cycles are shown for clarity. In the panel (d), 95% upper limits and net count rates (even zero net count rate) are shown in the first and second cycles, respectively, for bins with insignificant detection.

4850–8850 Å, but the last two had redder coverage, from 5950 to 9950 Å. These nine individual spectra all had exposure times of 1200 s. The Gemini spectra used the R400 grating, centered around 6800 Å, with a 1'' slit. All the exposures were 600 s. Fifteen spectra were obtained with Gemini; two of these Gemini spectra had signal-to-noise too low to be useful, but the remaining thirteen spectra were good. Both the SOAR and Gemini spectra were reduced and optimally extracted in the usual manner.

The immediate impression upon viewing the spectra is that the effective temperature of the star varies substantially over its orbit, and is quite warm when the “day” side of the star is facing Earth, suggesting the presence of heating. Comparing to the Paschen series of stars from the Ca triplet library of Cenarro et al. (2001), the Gemini spectra around  $\phi \sim 0.75$  are of the mid-A type, with effective temperatures around  $\sim 8000$  K. The Paschen series entirely disappears by the “night” phase of  $\phi \sim 0.25$ , where the relative strength of the metal to hydrogen lines are consistent with an early to mid G-type spectrum, with estimated temperatures of  $\sim 5700$  K (Figure 4). The spectra show no evidence of emission lines at any phase.

We determined barycentric radial velocities by cross-correlating the individual spectra with templates appropriate to their specific spectral types, primarily in the region of the Ca triplet and the Paschen series. These 22 velocities are listed as barycentric dynamical times in the TDB system (Eastman et al. 2010) in Table 3.

**Table 3**  
Barycentric Radial Velocities of 3FGL J0954.8–3948

BJD (days)	Radial Vel. (km s <sup>-1</sup> )	Unc. (km s <sup>-1</sup> )	Source
2457945.5057483	338.1	20.2	SOAR
2457956.4698649	86.6	21.3	SOAR
2457956.4838969	31.4	20.1	SOAR
2457956.4988242	-32.9	22.1	SOAR
2458072.7785401	-158.3	21.7	SOAR
2458072.7925358	-137.4	34.5	SOAR
2458072.8257413	-39.0	20.2	SOAR
2458095.7339401	180.2	8.5	Gemini
2458095.7425900	200.8	8.2	Gemini
2458095.7501254	249.8	7.6	Gemini
2458097.7417328	371.2	7.8	Gemini
2458102.7595228	349.6	7.1	Gemini
2458102.7681525	346.9	7.1	Gemini
2458102.7756881	362.7	7.4	Gemini
2458103.8328295	3.6	6.7	Gemini
2458103.8414655	56.2	6.8	Gemini
2458103.8507936	96.0	7.0	Gemini
2458106.7470583	122.3	9.8	Gemini
2458106.7557001	100.0	9.7	Gemini
2458106.7632348	71.0	8.9	Gemini
2458140.6035185	-81.1	23.9	SOAR
2458140.6175631	-22.2	20.1	SOAR

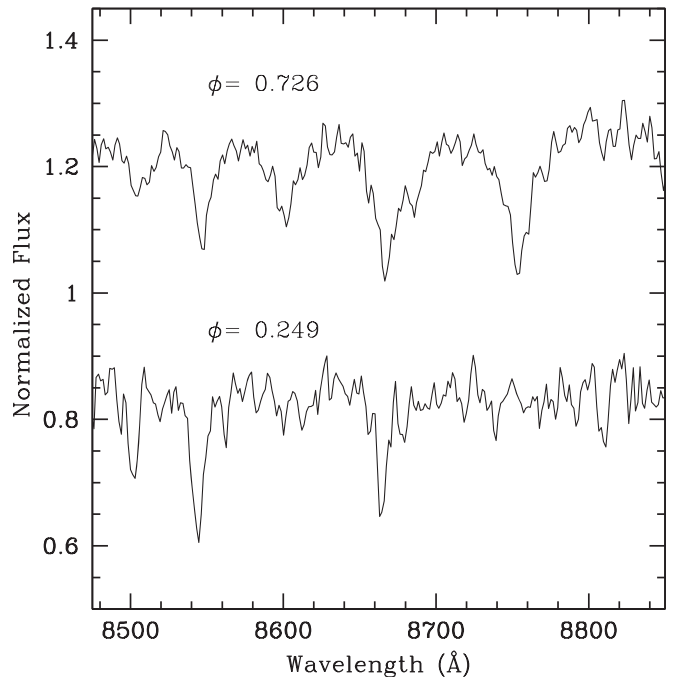


**Figure 4.** Gemini spectra of the star in the red near the extremes of the “day” ( $\phi = 0.73$ ) and “night” ( $\phi = 0.25$ ) side spectra, with the Paschen series evident on the day side and the Ca triplet on the night side.

We fit a circular Keplerian model to these radial velocities using the custom Markov Chain Monte Carlo sampler *The Joker* (Price-Whelan et al. 2017). The posterior distributions are approximately normal and uncorrelated. We summarize these with medians and equivalent  $1\sigma$  quantiles: period  $P_{\text{spec}} = 0.3873396(81)$  days, semi-amplitude  $K_2 = 272 \pm 4$  km s<sup>-1</sup>, systemic velocity  $\gamma = 96 \pm 3$  km s<sup>-1</sup>, and time of ascending node for the compact object

$T_{0,\text{spec}} = 2458097.94433 \pm 0.00053$  days. A fit with these median values has  $\chi^2/\text{d.o.f.} = 17.7/18$ , suggesting a reasonable fit. The orbital period is consistent with the CSS value (Section 4). Dropping the assumption of a circular orbit does not significantly improve the fit.

Assuming that the orbital period derivative over the period between the CSS and the SOAR/Gemini epochs is negligible (i.e., a stable period), we further constrain the orbital period by performing a joint fitting of the CSS photometric data and the radial velocities with a sinusoidal function and a cosinusoidal function (with the same period and  $T_0$  parameters shared), respectively. The best-fit orbital period is  $P_{\text{joint}} = 0.3873279(3)$  days with  $T_{0,\text{joint}} = 2458097.94395 \pm 0.00068$  days ( $\chi^2/\text{d.o.f.} = 134.9/202$ ). This more precise orbital solution was used in the UVOT and XRT timing analyses discussed in Sections 3 and 7.2, respectively (Figure 3). In addition, we tried fitting the data by allowing a “phase shift” between the CSS photometric light curve and the radial velocity curve, which is possible when the heating pattern is asymmetric. This gives  $P_{\text{joint},s} = 0.3873318(13)$  days with  $T_{0,\text{joint},s} = 2458097.94384 \pm 0.00068$  days and  $\Delta\phi = 0.08 \pm 0.03$  (i.e., the photometric peak at  $\phi = 0.83$ ;  $\chi^2/\text{d.o.f.} = 125.6/201$ ).

## 6. Radio Measurements in the Literature

Using the Giant Metrewave Radio Telescope (GMRT) 150 MHz All-Sky Radio Survey (TGSS ADR; Intema et al. 2017), Frail et al. (2016, 2018) identified radio pulsar candidates associated with unidentified *Fermi*-LAT sources in 2FGL, 3FGL, and preliminary 8-year source<sup>13</sup> catalogs. Three candidates were found within 2FGL sources, and one of these is associated with 3FGL J0954.8–3948. However, as the radio source is outside the 3FGL source’s 95% error ellipse, no detailed investigation was done.

The 3FGL J0954.8–3948-associated pulsar candidate is located at  $\alpha(\text{J2000}) = 09^{\text{h}}55^{\text{m}}27^{\text{s}}.75 \pm 2''.0$ ,  $\delta(\text{J2000}) = -39^{\circ}47'51''.1 \pm 2''.7$  ( $1\sigma$  uncertainty;  $2\text{DRMS} = 3''.4$ ), which is roughly consistent with the *Gaia* optical position of SSS J095527.8–394752 (the offset:  $2''.9$ ). This radio counterpart is a bright point source with 77 mJy at 150 MHz, but was cataloged neither in the Sydney University Molonglo Sky Survey (SUMSS at 843 MHz; Mauch et al. 2003) nor the NRAO VLA Sky Survey (NVSS at 1.4 GHz; Condon et al. 1998), indicating that it has a steep radio spectrum. Frail et al. (2016) estimated the spectral index to be  $\alpha \approx -1.6$  (where the flux density  $S_\nu \propto \nu^\alpha$ ), although it is highly uncertain given the poor flux constraints by SUMSS and NVSS. Nevertheless, this spectral index is fully consistent with that of a typical pulsar:  $\alpha = -1.60 \pm 0.03$ , the weighted mean spectral index of the 441 pulsars recently studied in Jankowski et al. (2018), for instance.

3FGL J0954.8–3948 is also one of the 56 targets in the Parkes radio MSP survey (Camilo et al. 2015). Unfortunately, no radio pulsation was found in a blind search with five 60 minute observations at 1.4 GHz. However, the offset between the optimized position of the radio search and the radio counterpart is as large as  $5'$ , which is comparable to the Parkes beam of  $7'.2$  (half-width at half-maximum; Camilo et al. 2015). This offset could have reduced the sensitivity of the search. Additionally, the radio pulsations could be eclipsed by the materials from the ablating companions during (some of) the observations. New search observations should be made at the updated position.

## 7. Discussion

In various aspects from radio through GeV  $\gamma$ -rays, we have shown that 3FGL J0954.8–3948 is well consistent with a redback MSP binary:

1. The system exhibited a clear orbital modulation in optical with a compact orbit of  $P = 9.3$  hr and  $K_2 = 272$  km s<sup>-1</sup>, which is common among the known redback systems.
2. The X-ray counterpart has a hard spectral index (i.e.,  $\Gamma_X \approx 1.4$ ) comparable to other redbacks, though the spectral index is uncertain, and deeper X-ray observations are needed.
3. The  $\gamma$ -ray flux is mostly stable on a monthly timescale and a significant curvature is found in the LAT spectrum. Both are signature features observed in many LAT-detected pulsars.
4. It has a pulsar-like radio counterpart with a steep spectral index of  $\alpha \approx -1.6$ .

These strongly suggest that the  $\gamma$ -ray source is a new redback MSP binary. We also comment that 3FGL J0954.8–3948 is unlikely to be a black widow MSP, since the source needs to be very nearby (i.e.,  $d = 200$  pc) to make the G-type secondary small in size (i.e.,  $\sim 0.1 R_\odot$ ). At this small distance, the X-ray and  $\gamma$ -ray luminosities would be as low as  $L_X \approx 1.5 \times 10^{30}$  erg s<sup>-1</sup> and  $L_\gamma \approx 8 \times 10^{31}$  erg s<sup>-1</sup>, which are far too low to produce the huge “day” and “night” temperature differences seen in the Gemini spectra (i.e.,  $L \sim 10^{34}$  erg s<sup>-1</sup> is required; will be discussed in Section 7.3). In addition, this close distance also contradicts the parallax of 3FGL J0954.8–3948 measured by *Gaia* (see Section 7.1). In contrast, a redback MSP scenario can provide a self-consistent picture for the multiwavelength observations.

### 7.1. Basic Properties of the Binary

The observed kinematics of the secondary yield the mass function  $f(M) = P_{\text{spec}} K_2^3 / (2\pi G) = M_1 (\sin i)^3 / (1+q)^2$  for gravitational constant  $G$ , inclination angle  $i$ , and mass ratio  $q = M_2/M_1$ . For SSS J095527.8–394752, we find that  $f(M) = 0.81 \pm 0.04 M_\odot$ . Assuming that the primary is a neutron star with a maximum mass of  $2.0 M_\odot$ , then the observed mass function implies  $i > 48^\circ$  (for  $M_1 = 1.4 M_\odot$ ,  $i > 56^\circ$ ). Given that most redbacks have secondaries with masses of at least  $0.2 M_\odot$ , the most likely range of the inclinations is somewhat more restricted,  $i > 52^\circ$  ( $M_1 = 2.0 M_\odot$ ) to  $i > 66^\circ$  ( $M_1 = 1.4 M_\odot$ ). Under these circumstances, the separation between the two binary members can be well restricted to  $a \sim (1.8\text{--}1.9) \times 10^{11}$  cm (equivalent to  $2.6\text{--}2.7 R_\odot$ ) for  $M_2 = 0.1\text{--}0.4 M_\odot$ .

Although not exclusively, normal redback systems often have luminosities of  $L_X \lesssim 10^{32}$  erg s<sup>-1</sup> (see, e.g., Linares 2014), putting a weak constraint of  $d \lesssim 1.7$  kpc on the distance for the redback MSP candidate. Another constraint comes from the parallax information from the second *Gaia* data release (GDR2; *Gaia* Collaboration et al. 2016, 2018),  $\varpi = 0.36 \pm 0.17$  mas (corrected for the global zero point of  $-0.029$  mas; Lindegren et al. 2018),<sup>14</sup> which can be converted to a geometric distance of  $d = 2.4^{+1.2}_{-0.7}$  kpc (probability contained: 68%; Bailer-Jones et al. 2018; Luri et al. 2018). Although these constraints are not totally consistent with each other, they both roughly agree

<sup>13</sup> <https://fermi.gsfc.nasa.gov/ssc/data/access/lat/fl8y/> (FL8Y)

<sup>14</sup> In GDR2, all parallaxes are computed by assuming that the sources are single stars. This could cause additional systematic uncertainties for binary systems.

$d \approx 1.7$  kpc. Assuming  $d = 1.7$  kpc, the  $V_{\text{css}} \sim 17$  mag G-type companion would have a radius of  $R_c \sim 0.7 R_\odot$ .<sup>15</sup> This stellar size is indeed in line with the fact that no obvious ellipsoidal variation is seen in the CSS light curve (average error: 0.3 mag), given that only weak ellipsoidal variability can be created by a  $R_c \sim 0.7 R_\odot$  secondary for 3FGL J0954.8–3948 (e.g., peak-to-peak amplitude  $\sim 0.4$  mag for  $M_1 = 1.4 M_\odot$  and  $M_2 = 0.4 M_\odot$ , computed with the ELC code; Orosz & Hauschildt 2000).

### 7.2. X-Ray Orbital Modulation?

To look for the X-ray modulation, we made an XRT light curve folded on the orbital period of  $P_{\text{joint}} = 0.3873279$  days (Figure 3). As we have mentioned in Section 3, the X-ray counterpart was not detected in every *Swift*-XRT observation. For better visualization, we plotted the bins with different colors based on whether the source was detected in a single full observation (detected: red; undetected: black). For all non-detection data bins, we present Bayesian bins (i.e., net count rates handled by a Bayesian approach, even for bins with zero net count rate; Kraft et al. 1991) in addition to 95% upper limits to scratch the possible orbital modulation in X-rays (Figure 3(d)).

While the black data set does not show evidence for a modulation, the red one is likely orbitally modulated with stronger X-ray emission seen in phase 0.6–0.8 (Figure 3(d)). This tentative X-ray peak seemingly aligns with the optical/UV peak at phase 0.75, which is the superior conjunction of the pulsar binary. Interestingly, X-ray modulation peaks around the superior conjunctions were commonly observed in redbacks, e.g., PSR J2129–0429 (Hui et al. 2015) and PSR J1723–2837 (Kong et al. 2017).

The poor data quality could be the reason to explain why the modulation was unseen in the black data set (see Section 3). Alternatively, it may imply a slightly unstable orbital modulation of the binary. In fact, it has been shown in PSR J1723–2837 that the X-ray orbital modulation of redback MSP binaries can change slightly from orbit to orbit due to, e.g., the wind instability of the companion (see Figure 1 in Kong et al. 2017). Further X-ray observations would remove the ambiguity.

#### 7.2.1. No Sign of Gamma-Ray Orbital Modulation

We also searched for possible  $\gamma$ -ray orbital modulation at  $>100$  MeV by folding the  $\gamma$ -ray photons accordingly. Different aperture radii from  $0^\circ$  to  $1^\circ$  were tried, but no evidence for an orbital modulation was found.

### 7.3. Interpretation for the High-energy Emission

Spin-down power is the major energy source for rotation-powered pulsars. Although the pulsations as well as the spin-down rate of 3FGL J0954.8–3948 have not been detected yet, we can still infer the spin-down power by measuring the pulsar irradiation on the companion, if the spin-down power and the irradiation power are approximately the same. With the

assumptions that the radiation/pulsar wind from the pulsar are both isotropic and the irradiated hemisphere of the companion is uniformly heated, the spin-down power of 3FGL J0954.8–3948 can be estimated from

$$\epsilon L_{sd} \sim \sigma_B (T_d^4 - T_n^4) \frac{2\pi R_c^2}{\delta\Omega}, \quad (1)$$

where  $\epsilon$  is the heating efficiency,  $\sigma_B$  is the Stefan–Boltzmann constant,  $T_d \sim 8000$  K and  $T_n \sim 5700$  K are the “day” and “night” temperatures, respectively, and  $\delta\Omega$  is the fraction of the sky covered by the companion star seen from the pulsar, which can be written as  $\delta\Omega \sim \pi(R_c/a)^2 \sim 0.47$  for  $a \sim 1.8 \times 10^{11}$  cm (corresponding to  $M_2 \approx 0.2 M_\odot$ ). The inferred spin-down power is  $L_{sd} \sim \frac{1}{\epsilon} \times 10^{34}$  erg s<sup>−1</sup>, a very typical value for MSPs.

Presumably, the X-ray and GeV  $\gamma$ -ray emission of 3FGL J0954.8–3948 originates from the intrabinary shock and the pulsar magnetosphere (Li et al. 2014; Takata et al. 2014; An et al. 2017) if it is a redback MSP, i.e., the shock-accelerated electrons and positrons emit X-ray/soft  $\gamma$ -rays via synchrotron radiation, and even TeV photons via inverse-Compton scattering off the stellar photons.

The outer-gap emission from the pulsar magnetosphere (Cheng et al. 1986) will contribute significantly in the LAT energy domain, especially above 1 GeV. We computed the outer-gap spectrum using the emission model developed by Wang et al. (2010) with the spin-down power of

$$L_{sd} = 3.8 \times 10^{35} \left( \frac{P_s}{1 \text{ ms}} \right)^{-4} \left( \frac{B_s}{10^8 \text{ G}} \right)^2 \text{ erg s}^{-1}, \quad (2)$$

which gives the strength of the surface dipole field  $B_s \sim 1.5 \times 10^8$  G for a spin period of  $P_s \sim 3$  ms and  $L_{sd} = 2 \times 10^{34}$  erg s<sup>−1</sup> ( $\epsilon \sim 0.5$  assumed). The magnetospheric emission from the outer gap is highly related to the gap fraction, i.e.,  $L_{\text{gap},\gamma} \sim f_{\text{gap}}^3 L_{sd}$ , where the gap fraction  $f_{\text{gap}}$  is defined by the ratio of the gap thickness to the light cylinder radius at the light cylinder. For MSPs, the gap fraction is empirically found to be  $f_{\text{gap}} > 0.3$ , as the LAT  $\gamma$ -ray luminosities are often  $>10\%$  of the spin-down powers (Abdo et al. 2013). In the model calculation for 3FGL J0954.8–3948, we assumed a gap fraction of  $f_{\text{gap}} \sim 0.5$  to explain the observed luminosity with  $d = 1.7$  kpc. As long as we fix the spin-down luminosity and the gap fraction, the predicted  $\gamma$ -ray luminosity is not sensitive to the spin period.

For the intrabinary shock contribution, we first roughly estimate the ratio of the momenta of the stellar wind and the pulsar wind ( $\eta_b$ ) from the X-ray light curve. It has been suggested that the X-ray orbital modulation of redback systems is caused by the Doppler boosting of the post-shocked wind (e.g., PSRs J1023+0038 and J2129–0429; Li et al. 2014; Kong et al. 2018). If the X-ray modulation of 3FGL J0954.8–3948 is genuine, then the shock cone has to be wrapping the pulsar such that the X-ray emission can be Doppler-boosted to create an X-ray flux maximum when the companion is behind the pulsar (phase = 0.75 in Figure 3). In this case, the stellar wind should have a larger momentum than the pulsar wind. We therefore assumed  $\eta_b = 7$ , which was also used to explain the X/ $\gamma$ -ray properties of the redback MSP J1023+0038 (Li et al. 2014). The shock geometry with  $\eta_b = 7$  is calculated with the method discussed by Canto et al. (1996), with the

<sup>15</sup>  $V_{\text{css}} \approx 17$  mag was inferred from the best-fit magnitude at night presented in Section 4 (without irradiation of the pulsar). An extinction correction with the best-fit  $N_H$  of  $5.2 \times 10^{21}$  cm<sup>−2</sup> obtained from X-ray spectral fitting (Güver and Özel 2009) has been applied. If  $N_H = 10^{21}$  cm<sup>−2</sup> is assumed, the  $V_{\text{css}}$  magnitude will increase to 18.6 mag (fainter) with a smaller inferred companion size of  $R_c \sim 0.3 R_\odot$ .

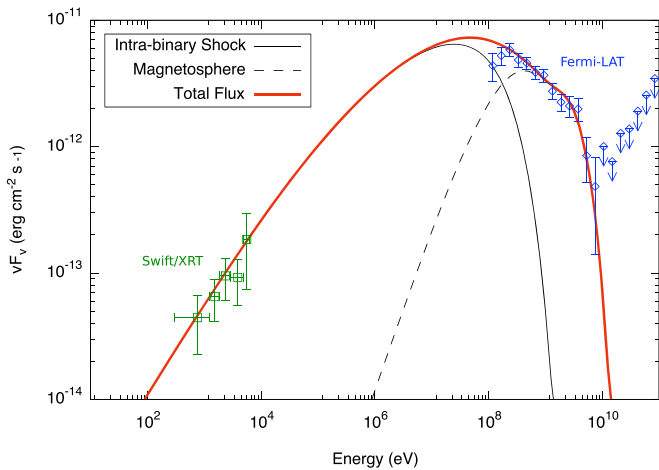


**Figure 5.** Spectral energy distribution of 3FGL J0954.8–3948 in the soft X-ray band (*Swift*-XRT; 0.3–10 keV; absorption corrected with  $N_{\text{H}} = 5.2 \times 10^{21} \text{ cm}^{-2}$ ) and the GeV  $\gamma$ -ray band (*Fermi*-LAT; 0.1–100 GeV). The solid and the dashed lines are the energy spectra from the intrabinary shock and the outer gap of the pulsar magnetosphere, respectively. See Section 7.3 for more details of the model.

magnetic field strength at the shock parameterized by the magnetization  $\sigma$ . Besides the shock geometry, this magnetization parameter also controls the X/ $\gamma$ -ray luminosities from the intrabinary shock once the spin-down power is fixed at a certain value (i.e.,  $L_{\text{sd}} = 2 \times 10^{34} \text{ erg s}^{-1}$ ), as the synchrotron luminosity is proportional to the square of the magnetic field strength, which depends on the magnetization as  $\sigma^{1/2}$ . For 3FGL J0954.8–3948, we applied  $\sigma = 0.1$  to match the observed X-ray luminosity.

The initial energies of the accelerated particles are assumed to be power-law distributed. The maximum energy of the particles is determined by balancing the synchrotron loss timescale and the acceleration timescale, yielding the Lorentz factor of  $\gamma_{\text{max}} = [9m_e^2 c^4 / (4e^3 B)]^{1/2}$  at maximum, while  $\gamma_{\text{min}} = 10^4$  is assumed for the minimum Lorentz factor. We finally solve the evolution of the energies of the particles under synchrotron radiation (inverse-Compton scattering loss is negligible for the MSP binaries) and calculate the corresponding intrabinary shock emission. Details of the calculation can be found in Takata et al. (2014) and Li et al. (2014).

Figure 5 shows the calculated emission components from the intrabinary shock and the outer gap, which match the *Swift*-XRT and *Fermi*-LAT spectra very well. Despite the ideal consistency, we emphasize that the parameter space for this system has not been fully explored, and therefore this specific parameter set is just one example that appears to fit the data. Additional measurements for the key parameters, such as  $L_{\text{sd}}$  and  $P_s$ , are essentially required to accurately capture the full physical behavior of the system in the future.

Note that Camilo et al. (2015) classified 3FGL J0954.8–3948 as a “poorer pulsar candidate” because of its “monotonically decreasing” (with energies) LAT spectrum, which is theoretically unfavored for a pulsar. With our intrabinary shock model, we have demonstrated that, even though the magnetospheric emission of a redback pulsar (the outer-gap model, for instance) peaks at  $\sim 1$  GeV (in the frame of  $\nu F_\nu$ ), the spectrum can be contaminated at low energies by the  $\sim 0.1$  GeV shock emission, making the  $\gamma$ -ray counterpart nonpulsarlike. Apparently,  $\gamma$ -ray

spectra are not good as a pulsar indicator alone when very strong intrabinary shock emission is observed.

#### 7.4. The Largely Shifted LAT Localization

We should not expect 100% accuracy for 95% error ellipses by definition; however, the case of 3FGL J0954.8–3948 is quite extreme—the 3FGL and the updated error regions are separated by  $6'$  and just barely touch each other by the edges (Figure 1), which may worth a brief discussion. We compared the 3FGL localization with the previous results in 1/2FGL; the 1FGL 95% error ellipse is big enough to encompass all the localizations, including the new best-fit position, while the ones in 2FGL (which has the X-ray/optical/radio counterpart inside) and 3FGL are more consistent with each other. To ensure the reliability of the new LAT localization, we visually checked the count map and the TS map, which both confirm the new best-fit position. Furthermore, our new error circle is almost identical to that in FL8Y (i.e., FL8Y J0955.4–3949; Figure 1).

Obviously, the great improvement is given by a much higher quality of data, as more than 9 years of Pass 8 data were used. At the same time, 3FGL J0954.8–3948 is a relatively bright and significant  $\gamma$ -ray source in 3FGL with a detection significance of  $19\sigma$ , reflecting that the unsatisfactory localization is unlikely to be caused by insufficient quality of the data used in the catalog. Strong variability of nearby sources can possibly affect the best-fit localization of an object; however, no cataloged variable  $\gamma$ -ray source can be found within  $4^\circ$  of 3FGL J0954.8–3948. Alternatively, the Galactic diffuse emission in this area may not be well modeled in 3FGL, leading to residual emission that could cause the offset. Though 3FGL J0954.8–3948 is about  $11^\circ$  away from the Galactic plane, there is still plenty of Galactic structure to make this scenario possible. Lastly, the relatively soft  $\gamma$ -ray spectrum of 3FGL J0954.8–3948 (the photon index is 2.54 in 3FGL; Acero et al. 2015) could also account for the underestimated positional uncertainty.

In any case, our *Fermi*-LAT study on 3FGL J0954.8–3948 clearly shows that the 95% error ellipses from the likelihood analysis can be underestimated sometimes, even for bright sources with significant detections. While we believe that most of the 3FGL error ellipses are still reliable, expanding the regions of interest slightly beyond the LAT error ellipses could be a wise strategy when identifying unassociated *Fermi*-LAT sources with multiwavelength observations.

The *Fermi*-LAT Collaboration acknowledges generous ongoing support from a number of agencies and institutes that have supported both the development and the operation of the LAT, as well as scientific data analysis. These include the National Aeronautics and Space Administration and the Department of Energy in the United States; the Commissariat à l’Energie Atomique and the Centre National de la Recherche Scientifique/Institut National de Physique Nucléaire et de Physique des Particules in France; the Agenzia Spaziale Italiana and the Istituto Nazionale di Fisica Nucleare in Italy; the Ministry of Education, Culture, Sports, Science and Technology (MEXT), High Energy Accelerator Research Organization (KEK), and Japan Aerospace Exploration Agency (JAXA) in Japan; and the K. A. Wallenberg Foundation, the Swedish Research Council, and the Swedish National Space Board in Sweden. Additional support for science analysis during the operations phase is gratefully acknowledged from



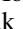
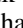
the Istituto Nazionale di Astrofisica in Italy and the Centre National d'Études Spatiales in France.

X.H. is supported by the National Natural Science Foundation of China through grants 11503078 and 11661161010. J.S. acknowledges support from a Packard Fellowship. Support from NSF grant AST-1714825 and NASA grant 80NSSC 17K0507 is gratefully acknowledged. J.T. is supported by the National Science Foundation of China (NSFC) under grants 11573010, U1631103, and 11661161010. A.K.H.K. is supported by the Ministry of Science and Technology of the Republic of China (Taiwan) through grant 105-2119-M-007-028-MY3. C.Y.H. is supported by the National Research Foundation of Korea grant 2016R1A5A1013277. K.S.C. is supported by GRF grant number 17302315.

Support for this work was partially provided by the National Aeronautics and Space Administration through *Chandra* Award Number GO7-18036X issued by the *Chandra* X-ray Observatory Center, which is operated by the Smithsonian Astrophysical Observatory for and on behalf of the National Aeronautics Space Administration under contract NAS8-03060. This work made use of data supplied by the UK Swift Science Data Centre at the University of Leicester. This work is also based on observations obtained at the Gemini Observatory (Program ID: GS-2017B-FT-15), which is operated by the Association of Universities for Research in Astronomy, Inc., under a cooperative agreement with the NSF on behalf of the Gemini partnership: the National Science Foundation (United States); the National Research Council (Canada); CONICYT (Chile); Ministerio de Ciencia, Tecnología e Innovación Productiva (Argentina); and Ministério da Ciência, Tecnologia e Inovação (Brazil). The CSS survey is funded by the National Aeronautics and Space Administration under Grant No. NNG05GF22G issued through the Science Mission Directorate Near-Earth Objects Observations Program. The CRTS survey is supported by the U.S. National Science Foundation under grants AST-0909182 and AST-1313422. This work has made use of data from the European Space Agency (ESA) mission *Gaia* (<https://www.cosmos.esa.int/gaia>), processed by the *Gaia* Data Processing and Analysis Consortium (DPAC, <https://www.cosmos.esa.int/web/gaia/dpac/consortium>). Funding for the DPAC has been provided by national institutions, in particular the institutions participating in the *Gaia* Multilateral Agreement.

*Facilities:* *Fermi*, *Swift*, SOAR, Gemini:South.

## ORCID iDs

Kwan-Lok Li  <https://orcid.org/0000-0002-0439-7047>  
 Xian Hou  <https://orcid.org/0000-0003-0933-6101>  
 Jay Strader  <https://orcid.org/0000-0002-1468-9668>  
 Jumpei Takata  <https://orcid.org/0000-0002-8731-0129>  
 Albert K. H. Kong  <https://orcid.org/0000-0002-5105-344X>  
 Laura Chomiuk  <https://orcid.org/0000-0002-8400-3705>  
 Samuel J. Swihart  <https://orcid.org/0000-0003-1699-8867>

## References

- Abdo, A. A., Ackermann, M., Ajello, M., et al. 2010, *ApJS*, 188, 405  
 Abdo, A. A., Ajello, M., Allafort, A., et al. 2013, *ApJS*, 208, 17  
 Acero, F., Ackermann, M., Ajello, M., et al. 2015, *ApJS*, 218, 23  
 Acero, F., Ackermann, M., Ajello, M., et al. 2016, *ApJS*, 223, 26  
 Alpar, M. A., Cheng, A. F., Ruderman, M. A., & Shaham, J. 1982, *Natur*, 300, 728  
 An, H., Romani, R. W., Johnson, T., Kerr, M., & Clark, C. J. 2017, *ApJ*, 850, 100  
 Archibald, A. M., Stairs, I. H., Ransom, S. M., et al. 2009, *Sci*, 324, 1411  
 Atwood, W., Albert, A., Baldini, L., et al. 2013, arXiv:1303.3514  
 Bailer-Jones, C. A. L., Rybizki, J., Fouesneau, M., Mantelet, G., & Andrae, R. 2018, arXiv:1804.10121  
 Bogdanov, S., & Halpern, J. P. 2015, *ApJL*, 803, L27  
 Camilo, F., Kerr, M., Ray, P. S., et al. 2015, *ApJ*, 810, 85  
 Camilo, F., Reynolds, J. E., Ransom, S. M., et al. 2016, *ApJ*, 820, 6  
 Canto, J., Raga, A. C., & Wilkin, F. P. 1996, *ApJ*, 469, 729  
 Cash, W. 1979, *ApJ*, 228, 939  
 Cenarro, A. J., Cardiel, N., Gorgas, J., et al. 2001, *MNRAS*, 326, 959  
 Chen, H.-L., Chen, X., Tauris, T. M., & Han, Z. 2013, *ApJ*, 775, 27  
 Cheng, K. S., Ho, C., & Ruderman, M. 1986, *ApJ*, 300, 500  
 Clemens, J. C., Crain, J. A., & Anderson, R. 2004, *Proc. SPIE*, 5492, 331  
 Condon, J. J., Cotton, W. D., Greisen, E. W., et al. 1998, *AJ*, 115, 1693  
 Drake, A. J., Djorgovski, S. G., Catelan, M., et al. 2017, *MNRAS*, 469, 3688  
 Drake, A. J., Djorgovski, S. G., Mahabal, A., et al. 2009, *ApJ*, 696, 870  
 Eastman, J., Siverd, R., & Gaudi, B. S. 2010, *PASP*, 122, 935  
 Evans, P. A., Beardmore, A. P., Page, K. L., et al. 2007, *A&A*, 469, 379  
 Evans, P. A., Beardmore, A. P., Page, K. L., et al. 2009, *MNRAS*, 397, 1177  
 Evans, P. A., Osborne, J. P., Beardmore, A. P., et al. 2014, *ApJS*, 210, 8  
 Frail, D. A., Mooley, K. P., Jagannathan, P., & Intema, H. T. 2016, *MNRAS*, 461, 1062  
 Frail, D. A., Ray, P. S., Mooley, K. P., et al. 2018, *MNRAS*, 475, 942  
 Gaia Collaboration, Brown, A. G. A., Vallenari, A., et al. 2018, arXiv:1804.09365  
 Gaia Collaboration, Prusti, T., de Bruijne, J. H. J., et al. 2016, *A&A*, 595, A1  
 Güver, T., & Özel, F. 2009, *MNRAS*, 400, 2050  
 Halpern, J. P., Strader, J., & Li, M. 2017, *ApJ*, 844, 150  
 Hui, C. Y., Hu, C. P., Park, S. M., et al. 2015, *ApJL*, 801, L27  
 Intema, H. T., Jagannathan, P., Mooley, K. P., & Frail, D. A. 2017, *A&A*, 598, A78  
 Jankowski, F., van Straten, W., Keane, E. F., et al. 2018, *MNRAS*, 473, 4436  
 Kalberla, P. M. W., Burton, W. B., Hartmann, D., et al. 2005, *A&A*, 440, 775  
 Kataoka, J., Yatsu, Y., Kawai, N., et al. 2012, *ApJ*, 757, 176  
 Kong, A. K. H., Huang, R. H. H., Cheng, K. S., et al. 2012, *ApJL*, 747, L3  
 Kong, A. K. H., Hui, C. Y., Takata, J., Li, K. L., & Tam, P. H. T. 2017, *ApJ*, 839, 130  
 Kong, A. K. H., Jin, R., Yen, T.-C., et al. 2014, *ApJL*, 794, L22  
 Kong, A. K. H., Takata, J., Hui, C. Y., et al. 2018, arXiv:1806.01312  
 Kraft, R. P., Burrows, D. N., & Nousek, J. A. 1991, *ApJ*, 374, 344  
 Li, K.-L., Kong, A. K. H., Hou, X., et al. 2016, *ApJ*, 833, 143  
 Li, K. L., Kong, A. K. H., Takata, J., et al. 2014, *ApJ*, 797, 111  
 Linares, M. 2014, *ApJ*, 795, 72  
 Linares, M., Miles-Páez, P., Rodríguez-Gil, P., et al. 2017, *MNRAS*, 465, 4602  
 Lindegren, L., Hernandez, J., Bombrun, A., et al. 2018, arXiv:1804.09366  
 Luri, X., Brown, A. G. A., Sarro, L. M., et al. 2018, arXiv:1804.09376  
 Mattox, J. R., Bertsch, D. L., Chiang, J., et al. 1996, *ApJ*, 461, 396  
 Mauch, T., Murphy, T., Buttery, H. J., et al. 2003, *MNRAS*, 342, 1117  
 Moretti, A., Campana, S., Mineo, T., et al. 2005, *Proc. SPIE*, 5898, 360  
 Nolan, P. L., Abdo, A. A., Ackermann, M., et al. 2012, *ApJS*, 199, 31  
 Orosz, J. A., & Hauschildt, P. H. 2000, *A&A*, 364, 265  
 Papitto, A., Ferrigno, C., Bozzo, E., et al. 2013, *Natur*, 501, 517  
 Patruno, A., Archibald, A. M., Hessels, J. W. T., et al. 2014, *ApJL*, 781, L3  
 Pletsch, H. J., & Clark, C. J. 2015, *ApJ*, 807, 18  
 Pletsch, H. J., Guillemot, L., Fehrmann, H., et al. 2012, *Sci*, 338, 1314  
 Price-Whelan, A. M., Hogg, D. W., Foreman-Mackey, D., & Rix, H.-W. 2017, *ApJ*, 837, 20  
 Roberts, M. S. E. 2013, in IAU Symp. 291, Neutron Stars and Pulsars: Challenges and Opportunities after 80 years, ed. J. van Leeuwen (Cambridge: Cambridge Univ. Press), 127  
 Romani, R. W. 2012, *ApJL*, 754, L25  
 Romani, R. W. 2015, *ApJL*, 812, L24  
 Romani, R. W., Filippenko, A. V., & Cenko, S. B. 2014, *ApJL*, 793, L20  
 Romani, R. W., & Shaw, M. S. 2011, *ApJL*, 743, L26  
 Roy, J., Ray, P. S., Bhattacharyya, B., et al. 2015, *ApJL*, 800, L12  
 Salvetti, D., Mignani, R. P., De Luca, A., et al. 2015, *ApJ*, 814, 88  
 Saz Parkinson, P. M., Xu, H., Yu, P. L. H., et al. 2016, *ApJ*, 820, 8  
 Stappers, B. W., Archibald, A. M., Hessels, J. W. T., et al. 2014, *ApJ*, 790, 39  
 Strader, J., Chomiuk, L., Cheung, C. C., et al. 2015, *ApJL*, 804, L12  
 Strader, J., Chomiuk, L., Sonbas, E., et al. 2014, *ApJL*, 788, L27  
 Strader, J., Li, K.-L., Chomiuk, L., et al. 2016, *ApJ*, 831, 89  
 Swihart, S. J., Strader, J., Johnson, T. J., et al. 2017, *ApJ*, 851, 31  
 Takata, J., Li, K. L., Leung, G. C. K., et al. 2014, *ApJ*, 785, 131  
 van den Heuvel, E. P. J., & van Paradijs, J. 1988, *Natur*, 334, 227  
 Wang, Y., Takata, J., & Cheng, K. S. 2010, *ApJ*, 720, 178  
 Wood, M., Caputo, R., Charles, E., et al. 2017, arXiv:1707.09551